

Journal of Geophysical Research: Oceans

RESEARCH ARTICLE

10.1002/2015JC011431

Key Points:

- Optical properties of the offshore Columbia River plume are investigated
- Plume-related optical properties vary in the cross-shore direction
- MODIS-derived empirical algorithms of surface salinity are evaluated

Correspondence to:

G. S. Saldías,
gsaldias@coas.oregonstate.edu

Citation:

Saldías, G. S., R. Kipp Shearman, J. A. Barth, and N. Tufillaro (2016), Optics of the offshore Columbia River plume from glider observations and satellite imagery, *J. Geophys. Res. Oceans*, 121, 2367–2384, doi:10.1002/2015JC011431.

Received 2 NOV 2015

Accepted 26 FEB 2016

Accepted article online 1 MAR 2016

Published online 9 APR 2016

Optics of the offshore Columbia River plume from glider observations and satellite imagery

Gonzalo. S. Saldías¹, R. Kipp Shearman¹, John A. Barth¹, and Nicholas Tufillaro¹¹College of Earth, Ocean, and Atmospheric Sciences, Oregon State University, Corvallis, Oregon, USA

Abstract The Columbia River (CR) is the largest source of freshwater along the U.S. Pacific coast. The resultant plume is often transported southward and offshore forming a large buoyant feature off Oregon and northern California in spring-summer—the offshore CR plume. Observations from autonomous underwater gliders and Moderate Resolution Imaging Spectroradiometer (MODIS) satellite imagery are used to characterize the optics of the offshore CR plume off Newport, Oregon. Vertical sections, under contrasting river flow conditions, reveal a low-salinity and warm surface layer of ~20–25 m (fresher in spring and warmer in summer), high Colored Dissolved Organic Matter (CDOM) concentration, and backscatter, and associated with the base of the plume high chlorophyll fluorescence. Plume characteristics vary in the offshore direction as the warm and fresh surface layer thickens progressively to an average 30–40 m of depth 270–310 km offshore; CDOM, backscatter, and chlorophyll fluorescence decrease in the upper 20 m and increase at subsurface levels (30–50 m depth). MODIS normalized water-leaving radiance ($nLw(\lambda)$) spectra for CR plume cases show enhanced water-leaving radiance at green bands (as compared to no-CR plume cases) up to ~154 km from shore. Farther offshore, the spectral shapes for both cases are very similar, and consequently, a contrasting color signature of low-salinity plume water is practically imperceptible from ocean color remote sensing. Empirical algorithms based on multivariate regression analyses of $nLw(\lambda)$ plus SST data produce more accurate results detecting offshore plume waters than previous studies using single visible bands (e.g., $a_{dg}(412)$ or $nLw(555)$).

1. Introduction

Coastal waters are optically complex systems [Schofield *et al.*, 2004], often influenced by large concentration of sediments and particulate and dissolved organic matter from rivers and estuaries [e.g., Milliman and Meade, 1983; Del Castillo *et al.*, 1999]. Coastal margins affected by high river outflow tend to have a proportionally large area influenced by freshwater [e.g., Shi and Wang, 2009; López *et al.*, 2012]. In the Amazon river plume, for instance, optical properties are strongly influenced by river-derived constituents at distances over 1000 km from the river mouth [e.g., Del Vecchio and Subramaniam, 2004]. These freshwater-influenced systems have high CDOM absorption, which tends to be inversely correlated with salinity, and poor correlation between CDOM and chlorophyll concentrations [Blough and Del Vecchio, 2002]. As a result of this characteristic biogeochemical composition, most river plumes possess a contrasting green-brownish color, which makes them readily distinguishable from ambient waters through satellite visible imagery [Klemas, 2012]. Satellite data, however, do not provide adequate information about the vertical structure of a plume (i.e., stratification and plume thickness) and/or the vertical distribution of associated optical properties. Because of this, subsurface in situ observations are an essential component in the study of river plumes.

The Columbia River delivers about three quarters of the total freshwater input along the U.S. west coast [Barnes *et al.*, 1972] and is the world's eighteenth largest river in terms of discharge [Kang *et al.*, 2013]. The seasonality of the river flow has been widely described—high discharge occurs during winter and spring (~10,000–15,000 $m^3 s^{-1}$), whereas the minimum flow takes place in late summer (~3000 $m^3 s^{-1}$) [e.g., Morgan *et al.*, 2005]. This freshwater outflow creates the Columbia River plume (CRP), a mesoscale buoyant feature with significant biogeochemical impacts on the coastal ecosystem [Hickey *et al.*, 2010]: the CRP transports dissolved and particulate matter, larvae, plankton, and contaminants for hundreds of kilometers in both alongshore and cross-shore directions [e.g., Barnes *et al.*, 1972; Peterson and Peterson, 2009], it possesses high nutrient content that enhances local production at multiple trophic levels [Kudela *et al.*, 2010]

and helps to sustain the ecosystem during delayed upwelling periods [Hickey and Banas, 2008], enhances zooplankton aggregations at the plume fronts [Peterson and Peterson, 2009], and plays a crucial role in the survival of juvenile salmon, providing food and refuge from predators [Litz et al., 2013]. Moreover, the plume inhibits iron limitation [Kudela and Peterson, 2009] and promotes the offshore export of biomass to the outer shelf and slope as well as the development of a chlorophyll shadow zone off northern Oregon [Hickey et al., 2010].

The CRP can be transported in different directions according to the interplay of the river flow and the seasonal pattern of wind stress and surface circulation [Hickey et al., 1998, 2005], and consequently, the plume is commonly located north (south) of the river mouth in fall-winter (spring-summer) [Thomas and Weatherbee, 2006]. In terms of its optical properties, a pioneering study by Pak et al. [1970] showed that the offshore plume's light-scattering field is consistent with its low salinity (~32) along a main axis extending ~190 km south from the river mouth in summer. Beyond this point, the tongue-shaped feature of the plume is lost presumably due to higher rates of particle sinking [Pak et al., 1970].

In spite of the efforts to characterize the regional progression of the CRP using satellite observations [Fiedler and Laurs, 1990; Thomas and Weatherbee, 2006], only a few studies have included in situ data to confirm its intrinsic low-salinity signal and its relationship with ocean color imagery [Palacios et al., 2009, 2012]. These works only covered the northern portion of the Oregon coast near the CR mouth, and consequently, did not cover the entire plume and any relevant topographic feature (e.g., Heceta Bank and Cape Blanco) influencing the regional circulation [e.g., Castelao and Barth, 2005; Kosro, 2005], and were limited in time to brief surveys. Since the scattering signal of the plume varies in the alongshore direction [Pak et al., 1970], it is absolutely necessary to take optical measurements in the offshore CRP, and for an extended period of time, to try to understand the role of the plume in the optics of the northern California Current System.

Here we present observations from underwater gliders and MODIS (ocean color and SST) imagery for seven upwelling seasons (2006–2012) describing the optics of the offshore CRP off Newport, Oregon. The unusually high resolution of our long-term synoptic glider transects provides a unique opportunity to study the optics of the offshore CRP in combination with MODIS imagery as it increases the probability of finding coincident observations. Our primary objective is to provide a descriptive characterization of the optical properties of coastal waters off Newport as they are modified by the presence of the offshore CRP, and to build empirical algorithms of MODIS-derived surface salinity (MDS). To our knowledge, there is no previous study characterizing the optics of the CRP using fine-scale measurements from underwater gliders.

Section 2 contains the data and methods. Sections 3 presents the major results regarding the optical characteristics of the offshore CRP from glider profiles and MODIS $nLw(\lambda)$, and MDS estimates off Newport. Section 4 contains the discussion, emphasizing the complex optical nature of the plume and the advantages of using glider measurements in combination with MODIS visible and thermal channels. Finally, a brief summary is presented in section 5.

2. Data and Methods

2.1. Glider Measurements

Cross-shore repeated glider surveys off Newport, Oregon (Figure 1), have been conducted from April 2006 to September 2014 by the Oregon State University Glider Research Group using a fleet of Slocum gliders (since 2006) [Schofield et al., 2007] and Seagliders (since 2008) [Eriksen et al., 2001]. Data coverage spanning the upwelling seasons of 7 years (2006–2012) is dense, ranging from 80 to 100% for a particular season (Table 1). Glider observations from Slocums in 2013 and 2014 were significantly reduced in comparison to previous years, and are not included in the present study. The gliders recorded pressure, temperature, conductivity, dissolved oxygen, optically derived Colored Dissolved Organic Matter (CDOM) fluorescence, particulate backscattering coefficient ($b_{bp}(660)$) in Slocums and $b_{bp}(650)$ in Seagliders, and chlorophyll *a* fluorescence (Chl *a*). A total of 933 days (89%) with glider data demonstrates the excellent temporal coverage of our observations during the upwelling seasons (Table 1). The Slocum sections are about 75 km long with the offshore limit at around 125.1°W, generally extending from the ~20 m isobath to the 1000–2000 m isobath in ~4 days (Figure 1a). The Slocum gliders operate to 200 m. Seagliders covered the farther offshore region reaching 128°W and operate up to 1000 m. Before the start of our glider line in 2006, the Newport Hydrographic line (NH-line) was historically sampled bimonthly (seasonally) with stations 18 (9)

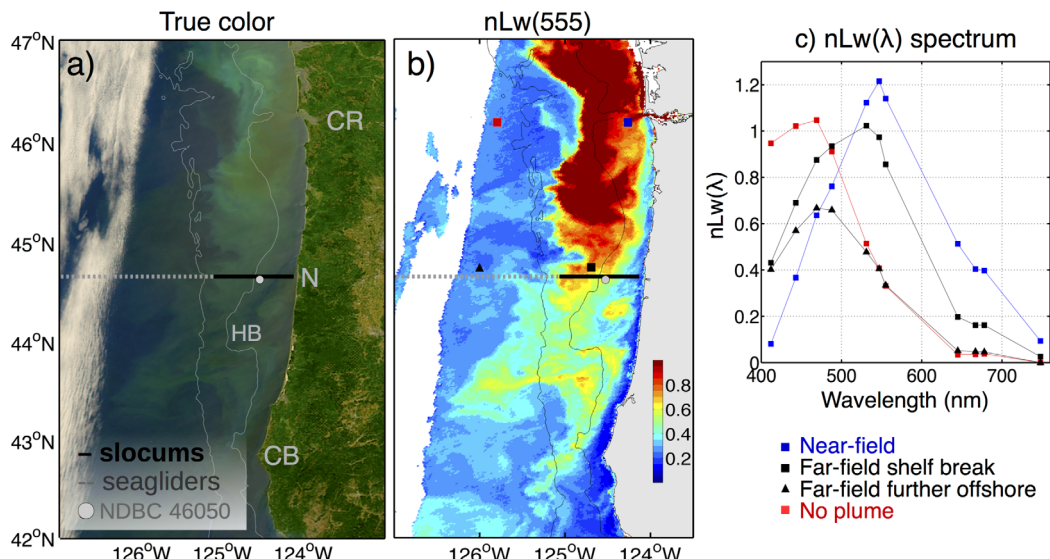


Figure 1. (a) Study area in a MODIS-Aqua true color image and (b) its corresponding $nLw(\lambda)$ signature at 555 nm ($\text{mW cm}^{-2} \mu\text{m}^{-1} \text{sr}^{-1}$), showing the offshore CRP on 27 June 2008. The $nLw(555)$ field has been normalized by the mean value at the CR mouth ($5 \times 10 \text{ km}$ box). The black (grey) line in Figure 1a indicates the glider cross-shelf trajectory. The grey dot off Newport represents the location of NDBC meteorological buoy 46050. Labels for Columbia River (CR), Newport (N), Cape Blanco (CB), and Heceta Bank (HB) are also included, and the 200 m and 2000 m isobaths are shown in grey and black lines in Figures 1a and 1b, respectively. The $nLw(\lambda)$ has been previously used as a tracer of particulate matter for the CRP [Thomas and Weatherbee, 2006]. The contrast of the true color image has been increased for a better visualization of the plume. Finally, the $nLw(\lambda)$ spectrum is presented in (c) for key locations specified in Figure 1b.

km apart over the continental shelf and 36 (18) km offshore (over the slope) during the years 1961–1971 (1997–2005) [Huyer et al., 2007]. Hence, our glider sections present the highest spatiotemporal resolution achieved in the region to date.

Temperature, conductivity, and pressure data were collected at 0.5 Hz, and subsequently cleaned by removing spikes. Salinity was estimated correcting the thermal lag error associated with CTD data [Garau et al., 2011]. The optical measurements are made through WET Labs Inc. Environmental Characterization Optics (ECO) Pucks mounted in the bottom of the gliders and facing downward. The measurements are in the form of raw voltages which are converted to the desired quantity by using the manufacturer calibrations and linear relationship:

$$[\beta(\theta_c), \text{Chl } a, \text{CDOM}] = SF * (\text{output} - DC) \quad (1)$$

$$SF = \chi / (\text{output}_\chi - DC) \quad (2)$$

$$SF = E(b_b(\lambda)/DC) * T(\beta(\theta_c)/b_b(\lambda)) \quad (3)$$

where SF (Scale Factor) from (2) and (3) is used in (1) for the computation of Chl a ($\mu\text{g L}^{-1}$) and CDOM (ppb) and total volume scattering ($\beta(\theta_c)$; $\text{m}^{-1} \text{sr}^{-1}$), respectively. χ in (2) is a known concentration of the

Table 1. Data Coverage for Gliders (Slocums, SI; Seagliders, Sg) and MODIS During the Upwelling Seasons^a

Years	Upwelling Season			Glider Coverage (Days)			MODIS Coverage Pixels (%)
	Start	End	Days	SI (Days)	Sg (Days)	SI + Sg (%)	
2006	18 Apr	1 Nov	198	170		170 (85)	44
2007	27 Apr	28 Sep	155	125		125 (80)	36
2008	3 May	15 Sep	136	101	83	115 (84)	27
2009	14 May	12 Oct	152	119	89	136 (89)	34
2010	10 Jun	15 Sep	98	73	56	81 (82)	28
2011	16 Apr	11 Sep	149	110	133	149 (100)	35
2012	4 May	7 Oct	157	135	157	157 (100)	36
Total			1045	833	518	933 (89)	35

^aMODIS coverage represents the percentage of cloud-free pixels (area limited 5 km north and south of the glider line).

constituent (Chl *a* or CDOM), $output_{\chi}$ is the measured signal output for the known concentration χ , $b_b(\lambda)$ in (3) is the total backscattering coefficient (m^{-1}), DC (Dark Counts) is the signal in the absence of light (measured signal output with black tape over the detector), and $output$ is the measured signal output during field sampling. E and T in (3) are used for denoting experimental and theoretical fractions, respectively. From $\beta(\theta_c)$, it is possible to obtain the volume scattering of particles (β_p) by subtracting the volume scattering of water (β_w) [Morel, 1974]. Then β_p is used to compute the particulate backscattering coefficients ($b_{bp}; m^{-1}$) and total backscattering coefficients ($b_b; m^{-1}$) following Boss and Pegau [2001]. Here $b_{bp}(\lambda)$ is referred simply as backscatter. Manufacturer calibrations of our ECO Pucks were performed every 2 or 3 years. A detailed description of these optical computations is found in the official WET Labs website (<http://www.wetlabs.com/eco-triplet>). Additional information about manufacturer's calibration of ECO Pucks' fluorometric measurements is found in Cetinić *et al.* [2009].

2.2. MODIS Imagery

Ocean color imagery from MODIS onboard the Aqua and Terra satellites was used to detect and track the surface signature of the plume during the upwelling season. All satellite images, for the years 2006–2012, were processed from L1 files (reprocessing V2012.0) using the NASA's software SeaDAS (SeaWIFS Data Analysis System version 6.4; <http://seadas.gsfc.nasa.gov/>) for the coastal region off Oregon/southern Washington between 42°N and 47°N and 128°W and 123°W. The processing was achieved using default atmospheric corrections [Gordon, 1997] and flags for producing daily images at 1 km spatial resolution. Although it is well recognized that the black pixel assumption does not hold when using NIR (near infrared) bands for corrections in turbid waters, and consequently the use of other bands as SWIR (short wave infrared) are recommended [Wang and Shi, 2007], we opted for maintaining default (NIR) settings for two reasons: (1) the implementation of SWIR bands in SeaDAS increased the noise and missing data of final products in our region of study; and (2) the offshore CRP shows a decreased level of turbidity as compared to the near-field area. The processing of the satellite imagery included all the visible spectrum of normalized water-leaving radiance ($nLw(\lambda); mW cm^{-2} \mu m^{-1} sr^{-1}$) at 412, 443, 469, 488, 531, 547, 555, 645, 667, and 678 nm, light absorption by colored dissolved and detrital matter at 412 nm ($a_{dg}(412)$) from the Garver-Siegel-Maritorena (GSM) model [Maritorena *et al.*, 2002], sea surface temperature (SST), and normalized Fluorescence Line Height (nFLH) [Behrenfeld *et al.*, 2009]. Here we do not include $nLw(\lambda)$ data from MODIS-Terra when doing analyses of all spectrum of radiance as most blue bands can be highly biased [Franz *et al.*, 2007]. Daily composites of $nLw(555)$ were used in combination with the glider observations for identifying match-up periods with and without the CRP influence. Fields of $nLw(555)$ from SeaWIFS have been previously used to map the surface expansion of the plume through the annual cycle [Thomas and Weatherbee, 2006]. MODIS images of $a_{dg}(412)$ and SST were used in the evaluation of a synthetic salinity product [Palacios *et al.*, 2009]. All images are mapped in a cylindrical projection.

2.3. Wind, River Discharge, and Sea Level Data

Daily river discharge data were obtained from USGS Oregon Water Science Center at the Beaver Army Terminal, Quincy, Oregon (<http://waterdata.usgs.gov/usa/nwis/uv>), and hourly data of wind speed and direction for buoy 46050 and the station NWPO3 at Newport (Figure 1) were obtained from the NOAA National Data Buoy Center (NDBC) website (<http://www.ndbc.noaa.gov>). NWPO3 data were used to fill gaps in the time series from buoy 46050 by fitting a regression model during each upwelling season [e.g., Kirincich *et al.*, 2005]. Neutral wind stress was computed following Large and Pond [1981]. Wind data were low-pass filtered with a half-power point of 40 h. The upwelling seasons (spring-summer) were defined between the spring to fall transition of each year according to the cumulative wind stress curve [Pierce *et al.*, 2006] (see <http://damp.coas.oregonstate.edu/windstress>). We also computed the adjusted sea level (ASL) in order to confirm the drop in coastal sea level as response to the upwelling process [Kosro *et al.*, 2006]. The coastal water level and atmospheric pressure data for the computation of the ASL were obtained from the tide gauge nearby South beach (<http://tidesandcurrents.noaa.gov>) and the NDBC station NWPO3 at Newport, respectively. The upwelling season start and end dates are given in Table 1.

2.4. Match-Up Procedure and Regression Analyses

All MODIS imagery (i.e., $nLw(\lambda)$, $a_{dg}(412)$, and SST) were smoothed using a two-dimensional (3×3 pixels) median filter to reduce noise mostly associated with cloud edges. This type of filter is routinely applied in order to reduce noise and enhance frontal features in satellite images [e.g., Wall *et al.*, 2008]. Coincidental

Table 2. Match-Up (No Days) Between Gliders (Slocums, SI; Seagliders, SG) and MODIS (MD) During the Upwelling Seasons

Years	CRP Cases			No-CRP Cases		
	SI – MD	Sg – MD	SI + Sg – MD	SI – MD	Sg – MD	SI + Sg – MD
2006	11		11	5		5
2007	10		10	0		0
2008	8	17	20	4	0	4
2009	6	11	16	1	0	1
2010	12	12	17	0	2	2
2011	12	22	28	0	3	3
2012	6	17	21	1	7	8
Total	65	79	123	11	12	23

concomitant observations considerably. All glider profiles within the area of a given pixel were averaged so that there is a unique set of values for that particular pixel. These steps are repeated for all pixels containing coincidental glider trajectories. The number of match-up days for both CRP and no-CRP cases is presented in Table 2.

Multivariate regression analyses [Emery and Thomson, 2004] were performed between glider salinity (at different layers) and surface optical data from three sources; MODIS $nLw(\lambda)$, MODIS $nLw(555)$, and MODIS $a_{dg}(412)$. The latter one has been used to predict surface salinity in the near-field plume [Palacios et al., 2009]. As the plume shows a strong temperature signal, SST was also included in addition to the optics. We computed surface salinity from the best regression results to evaluate the performance of the synthetic salinity algorithm (based on $a_{dg}(412)$ plus SST), the commonly used $nLw(\lambda)$ at 555 nm (based in $nLw(555) + SST$), and a MODIS-derived salinity (MDS) product (based on $nLw(\lambda)$ plus SST) for predicting surface salinity off Newport. For a particular longitudinal extension off Newport (see Figure 6), two different regression models were finally computed. The use of each model depended on the corresponding daily river discharge value (if greater or lower than a river flow threshold Q). This approximation produced better time series of predicted surface salinity than only using a single model. The best threshold value was found in each case by testing all possible river flows from 4000 to 9000 $m^3 s^{-1}$ and correlating the resultant salinity time series from the gliders and MODIS bands. This multiband approach using MODIS imagery has been previously applied elsewhere [e.g., Qing et al., 2013], and a detailed description of the computation steps is found in Marghany and Hashim [2011].

2.5. Additional Hydrographic Observations

Additional hydrographic data from CTD profiles for NH-line and NH10 mooring (44.64°N 124.3°W at ~80 m isobath) were included in order to evaluate the performance of the MDS algorithms off Newport. The CTD data were collected through the GLOBEC Northeast Pacific Long Term Observation Program (LTOP) and are available on the NOAA's coastwatch website (<http://coastwatch.pfeg.noaa.gov/erddap/tabledap/erdNewportCtd.html>). These data are available for the years 1997–2008 but here we only used concomitant data with MODIS observations (2002–2008). Surface salinity data from NH10 correspond to the period 2006–2012. This data set is included because is the longest salinity time series off Newport and also low-salinity pulses were recorded at midshelf during a couple of upwelling seasons, suggesting the influence of the CRP. The evaluation of the MDS estimates are presented in Figures 11 and 12 through the comparison of daily match-ups (only for NH10) and seasonal cycles of surface salinity (upwelling season; April to October).

3. Results

3.1. Basic Optical Characteristics From MODIS $nLw(\lambda)$

The optical characteristics of the CRP are highly distinct from adjacent ambient waters (Figure 1). The green-brownish color allows tracking the CR plume southward for a large distance (~300 km). This example is a fairly common pattern for the offshore CR plume and its signature reaches the line of glider sampling. The high signal from the $nLw(555)$ corroborates the southward extension of the plume during this event (Figure 1b) which was preceded by upwelling-favorable wind stress for 5 days and high river discharge (~11,860 $m^3 s^{-1}$). Also, contrasting spectral shapes exist among the near field, far field, and the farther offshore ocean presumably with reduced influence of the plume (Figure 1c). Note that here we use the term

MODIS and glider data were then obtained matching glider profiles to MODIS-Aqua within a 6 h window (3 h before and after the satellite passes at each day). A 6 h window is common in studies performing satellite—in situ data analysis, and produced increased number of match-ups off Newport—the reduction of this time window decreases our

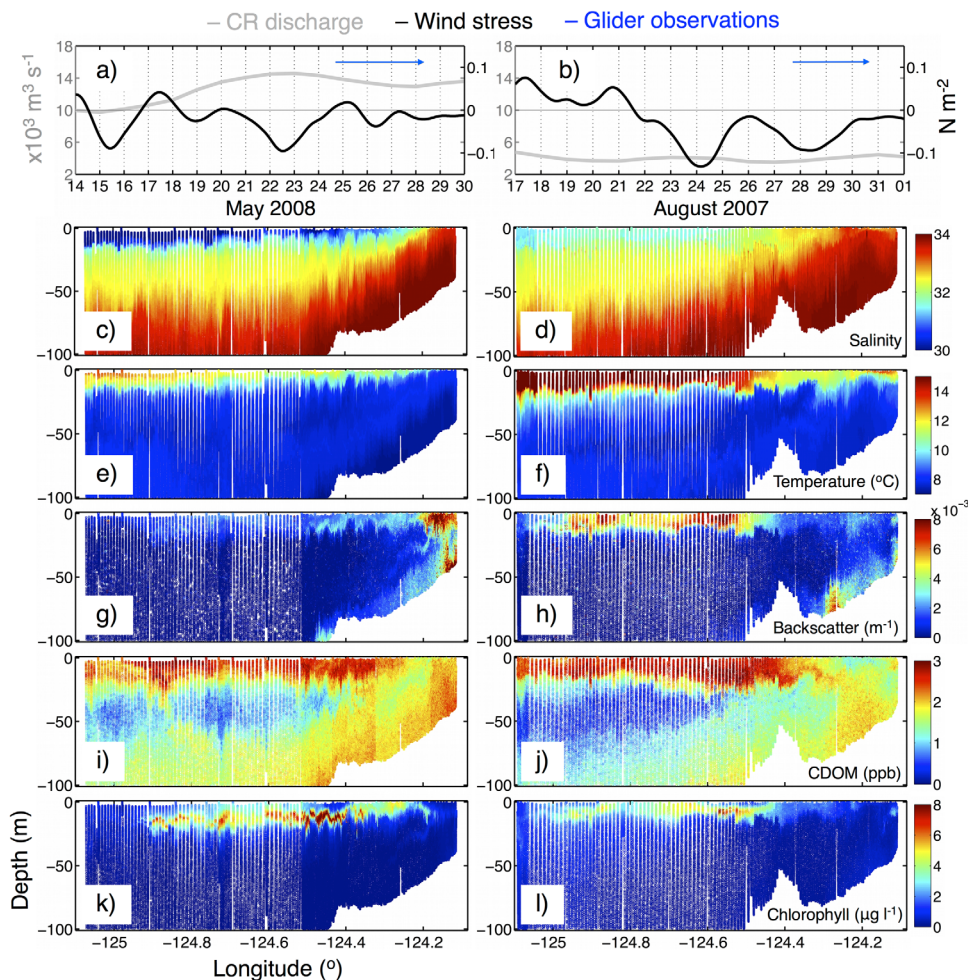


Figure 2. Examples of Slocum glider sections with the presence of the offshore CRP under contrasting river discharge conditions. Left (right) plots correspond to an event with high (low) river flow in relation to its annual cycle. (a and b) River flow and wind stress data during and previous to the glider observations are shown. Note that the time of glider observations are denoted with a blue arrow in Figures 2a and 2b. Glider data show (c and d) salinity, (e and f) temperature, (g and h) backscatter, (i and j) CDOM fluorescence, and (k and l) chlorophyll *a*.

far field for the region off Newport, whereas the general river plume terminology applies this term to the region far from the river mouth but in the opposite direction (downstream direction following the propagation of a Kelvin wave). Plume signatures have higher $nLw(\lambda)$ in the green bands whereas clear offshore waters peak in the lower part of the spectrum. The far-field plume near the shelf break has higher $nLw(\lambda)$ (less water absorption) in the blue bands than in the near-field plume, but maximum values still appear at some green bands for this particular example (Figure 1c). The far-field plume farther offshore shows a curve similar to the clear no-plume case, but $nLw(\lambda)$ in the blue side of the spectrum is comparably reduced, which suggests less plume influence—these decreased $nLw(\lambda)$ values are concordant to the high absorption of CDOM and other detritus materials from terrestrial sources.

3.2. Examples of the Offshore CRP in Cross-Shore Glider Sections

Cross-shore glider transects recorded many appearances of the CRP through the 7 years of study, however, here we only present results from the glider trajectories that are concordant with clear MODIS $nLw(555)$ fields identifying both the presence and absence of the CR plume. The MODIS imagery also revealed that some events with low-salinity water were consistent with the signal from the small local rivers of central Oregon [Mazzini et al., 2014] under upwelling conditions and mostly during early spring. Thus, glider data suggesting the presence of the CR plume but not supported by a clear MODIS image showing the presence of the CR plume were discarded in order to avoid the inclusion of glider data under the influence of these

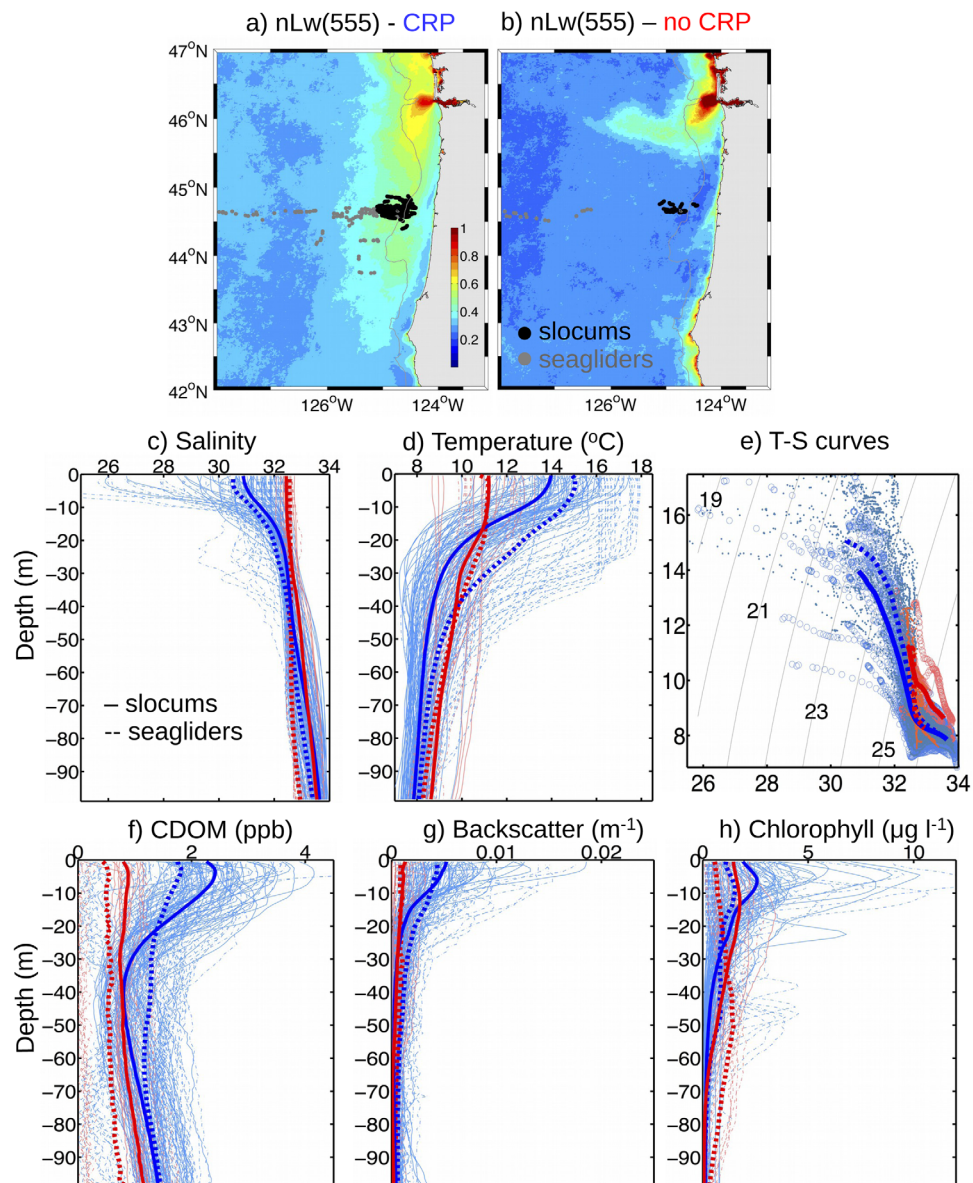


Figure 3. MODIS average nLw(555) imagery for match-up days with the (a) presence and (b) absence of the offshore CRP. Glider trajectories correspond to black (grey) dots for Slocums (Seagliders), where each dot is a daily event. All average daily profiles from matched glider measurements are presented in blue (presence of the offshore CRP) and red (absence of the offshore CRP) for each variable ((c) Salinity, (d) temperature, (e) T-S curves, (f) CDOM, (g) backscatter, and (h) chlorophyll). T-S curves for all daily profiles are presented in Figure 3e for better representation of the presence and absence of the offshore CRP off Newport. Open circles (dots) correspond to Slocums (Seagliders), whereas blue (red) is used for denoting the presence (absence) of the offshore CRP. Solid (dashed) lines correspond to Slocums (Seagliders) profiles. Profiles and T-S curves in bold correspond to average profiles for all respective match-ups.

small rivers. Two examples of glider transects under different river discharge conditions and recording the influence of the CR plume off Newport are presented in Figure 2. The upwelling state is characterized by several days with southward wind stress that promotes the southward and offshore advection of the plume through the upwelling season. Strong southward surface currents ($\sim 0.5\text{--}1 \text{ m s}^{-1}$) around the shelf break are typical for the upwelling jet during active upwelling [e.g., Barth *et al.*, 2005; Kosro, 2005]—these velocities imply that new plume water can be transported from the river mouth to the NH-line in approximately 2.4–5 days. As expected, high (low) river discharge early (late) in the upwelling season produces a plume with surface salinity values <30 ($\sim 31.5\text{--}32.5$) off Newport. In both cases the thickness of the plume spans ~ 20 m. Temperature in the plume is higher in summer (Figure 2f). As a result, the plume is fresher (less fresh) and less warm (warmer) early (late) in the upwelling season. In general, the optics of the surface layer

(0–20 m) show high backscatter and CDOM as compared to deeper levels. CDOM, however, seems to present a more coherent distribution with the low-salinity water than the backscatter in the surface 20 m. High CDOM concentration also appears near the bottom (but lower than in the plume) and reaches the surface in the inner shelf (bottom depth ≤ 50 m) (Figures 2i and 2j). Finally, high chlorophyll fluorescence characterizes the plume and extends to the surface at the frontal boundary between the inner edge of the plume and the upwelling front; where the front is defined by the salinity field (Figures 2k and 2l).

3.3. Plume Versus No-Plume Optics

For the purpose of contrasting optical characteristics between the offshore CRP and ambient waters in the region, match-ups between glider measurements and MODIS $nLw(555)$ imagery were identified for both the presence of the offshore CRP and the absence of any turbid plume (Figure 3). The presence of the plume, which shows a clear southward extension along most of the Oregon coast (Figure 3a), is associated with a fresher and warmer surface (~ 20 m) layer, with high CDOM, backscatter, and chlorophyll. The buoyant character of the plume is illustrated through the T-S curves where the CR plume case is extended on average until the $\sim 23 \text{ kg m}^{-3}$ isopycnal, whereas the average curve for the case without the plume only reaches the $\sim 25 \text{ kg m}^{-3}$ isopycnal (Figure 3e). From the average profiles (curves in bold), it is possible to infer that the plume has some influence even below the surface 20 m of depth.

The average CDOM profile from Slocums is minimum around 35–40 m (Figure 3f). It is also important to note that besides the clear high signal of CDOM and backscatter in the surface layer, the CR plume case presents a shallower surface peak in chlorophyll (Figure 3h), which is coherent with a shallower surface mixed layer when the plume is present. Clear thermal and optical differences appear between Slocum and Seaglider profiles, especially for the CRP case (blue curves), due to cross-shore differential structure. The average profiles show that, farther offshore and in comparison to Slocums profiles close to the shelf break, plume water is warmer (Figure 3d), CDOM is reduced at the surface and is vertically more uniform (Figure 3f), and Chl a is decreased at the surface (Figure 3i). Even though there is a large cross-shore extension covered by the gliders, the average no-CRP case from both Slocums and Seagliders (red lines) agreed well in temperature, salinity, and backscatter (Figures 3d, 3e, and 3h), and in a less extent in CDOM which present a clear offset (Figure 3f). To further clarify the effect of cross-shore distance involved in the averages, average profiles were generated grouping all data in segments of half a degree of longitude, and these are presented in the next section.

3.4. Cross-Shore Variability of Optical Properties

Cross-shore averages (Figure 4) for all CRP match-ups reveal a very distinct vertical structure depending on the cross-shore position. First, the freshwater surface layer is deeper farther offshore with more than 30 m of low-salinity water—note that low salinity peaks at the base of mixed layer in the two farther offshore bins. This is consistent with a warmer surface layer that shallows in the inshore direction for the CRP case. Notice that the halocline also tends to shallow in the inshore direction which is most likely the result of the upward tilting of isolines associated with upwelling. Similarly, the optics show contrasting patterns as a function of cross-shore distance; CDOM, backscatter, and Chl a present surface maxima in agreement with the low-salinity (and high temperature) layer for the inshore region between the 125.5°W and 124.4°W . As the offshore distance increases (more negative longitudes in the figure), these surface peaks decrease and subsurface peaks appear in all three variables, being more evident for Chl a and CDOM. Overall, peaks for locations farther offshore than 126°W are not associated with the offshore CRP water, but instead, farther below or near the mixed layer depth.

The no-CRP case shows a contrasting cross-shore structure with low variability in all variables, except for Chl a . When the offshore CRP is not present off Oregon, the vertical profiles are nearly homogeneous. The main differences for optical properties between CRP and no-CRP cases are found inshore of 125.5°W and farther offshore than 127°W , with the exception of Chl a showing similar profiles with peaks around 40–50 m depth.

This cross-shore differential distribution of optical properties in the offshore CRP is complemented with the cross-shore MODIS $nLw(\lambda)$ spectra in order to assess how the farther offshore deepening of optical peaks is seen by MODIS (Figure 5). For comparison, the $nLw(\lambda)$ off the CR is also shown. Also, the farther offshore region from the CR is rarely impacted by the plume as this is mainly transported in the north-south

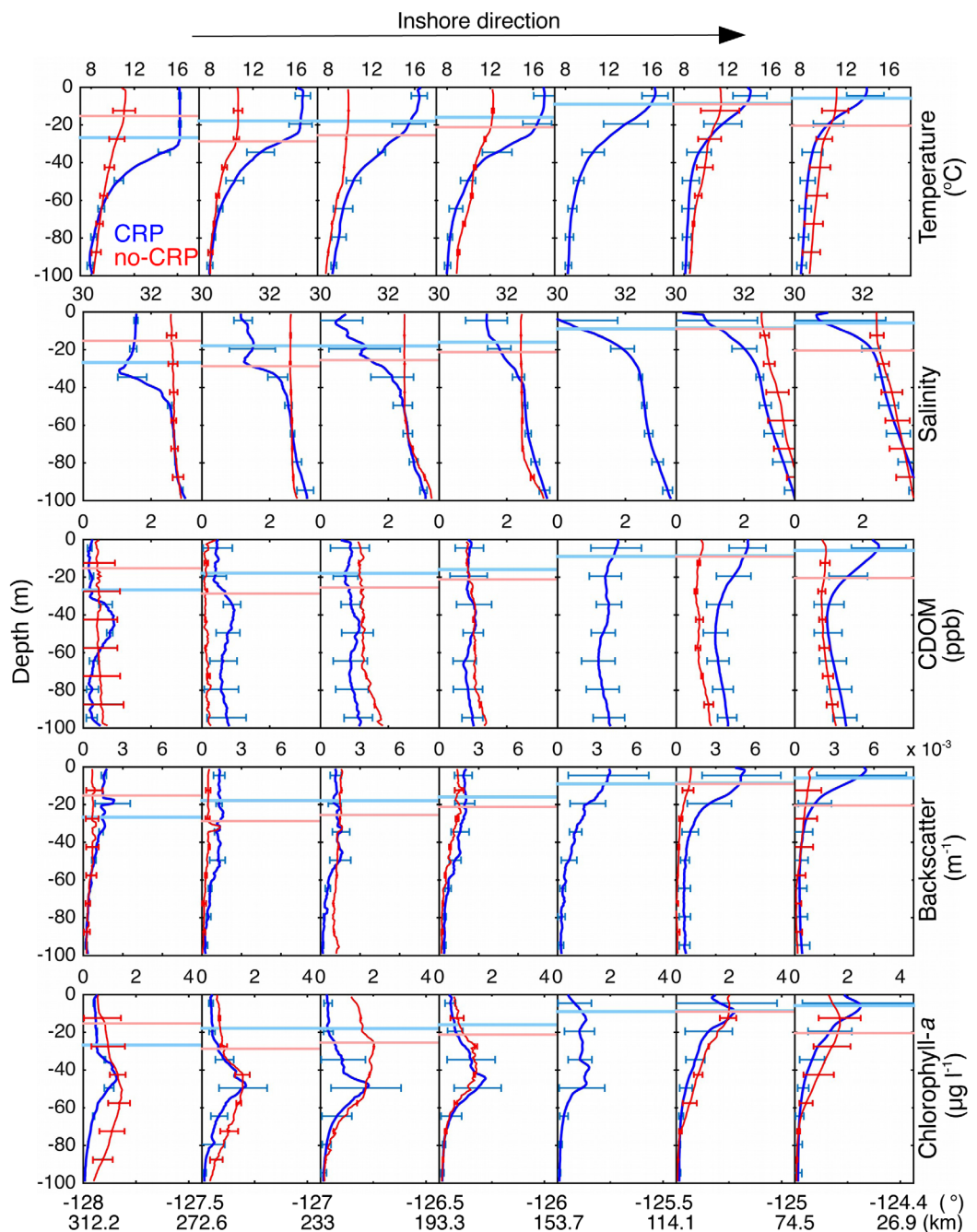


Figure 4. Cross-shore vertical structure of temperature, salinity, and optical measurements for all CRP (blue lines) and no-CRP (red lines) cases grouped in segments of half a degree. Horizontal error bars are plus/minus the standard deviation of average profiles. The mean mixed layer depths (CRP versus no-CRP), based on potential density profiles [Holte and Talley, 2009], are indicated by horizontal lines. Note that the limits of longitude and distance offshore are presented at the bottom.

direction. Thus, its spectrum serves as reference for comparison with the far-field case off Newport. When the offshore CRP is formed, the near-field area has increased $nLw(\lambda)$ at the green bands, however, the maximum values are not centered on the $nLw(555)$ but instead at the 531–547 nm bands. This optical signature is fairly consistent inshore of 124.5°W. A transitional region can then be identified up to ~125°W where maximum $nLw(\lambda)$ moves to lower bands in the blue, whereas the farther offshore region shows clear “open ocean” waters with typical $nLw(\lambda)$ spectra characterized by maxima in the blue and a rapid decrease toward higher wavelengths (Figure 5a). Notable differences are found off Newport, where now the maximum values at 531 and 547 nm are confined approximately between 125°W and 124.5°W, the transitional

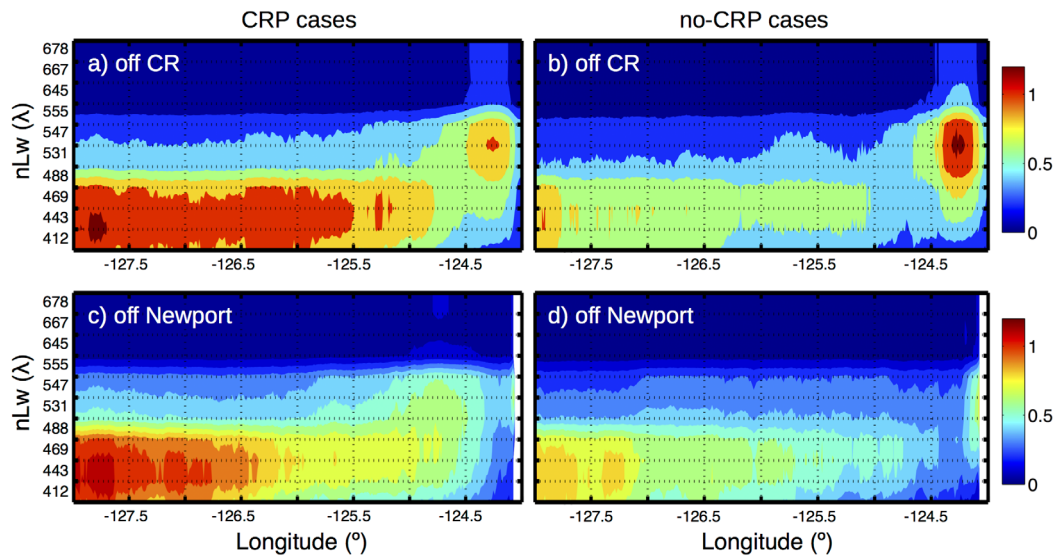


Figure 5. Cross-shore average $nLw(\lambda)$ spectra ($\text{mW cm}^{-2} \mu\text{m}^{-1} \text{sr}^{-1}$) off (top) CR mouth and (bottom) Newport for both (left) CRP and (right) no-CRP match-up cases as defined by presence or absence of CRP off Newport.

region (identified by the sloping isolines) reaches the $\sim 126^{\circ}\text{W}$ – 126.5°W , and a well-defined low turbid “open ocean” spectrum is found farther offshore of $\sim 126.5^{\circ}\text{W}$ (Figure 5c). This cross-shore $nLw(\lambda)$ structure is consistent with the glider measurements (Figure 4) as the lack of high optical values in the surface low-salinity layer is seen as clear waters by MODIS. The no-CRP cases show that the near-field region is much more turbid than when the offshore CRP is formed, and also the offshore region presents lower $nLw(\lambda)$ values in the blue bands (Figure 5b). Finally, a similar offshore $nLw(\lambda)$ spectra to the case off CR are observed off Newport (no-CRP cases) with decreased values for the 412–443–469 nm, and also, the relatively flat isolines confirm the absence of the offshore CRP without any green maxima (Figure 5d). Standard deviation plots of $nLw(\lambda)$ spectra (not shown) confirm a low variability of the offshore region in the green and red parts of the spectrum when the offshore CRP is well developed—the clear ocean characterization westward of $\sim 126^{\circ}\text{W}$ is persistent in most events.

3.5. MODIS-Derived Surface Salinity (MDS) Off Newport

To further explore the relation of optical conditions to salinity during spring-summer, multivariate regression analyses are used to estimate salinity from MODIS bands. In most cases, the inclusion of SST improves the prediction of salinity, especially in the surface layers (up to 10–15 m), and consequently MODIS SST data are also included in the analyses. Results from the correlations of MDS with glider salinity are presented in Figures 6 and 7. Considering the high cross-shore variability in optical properties from Figures 4 and 5, the regressions were estimated for segments of longitude (cross-shore distance) producing the best surface estimates of salinity. As expected, these segments become shorter in the inshore direction. MDS was highly correlated to glider salinity in the surface 10 m but the correlation progressively decreases shoreward (Figure 6). Accurate estimates of salinity farther offshore (128°W – 126°W) are achieved by all bands used—MDS based on $nLw(\lambda)$, $a_{dg}(412)$, and $nLw(555)$ all have the same pattern with high correlation with glider salinity at surface and decreasing smoothly with depth (Figure 6a). In the inshore direction, surface correlation coefficients are better for the cases using $nLw(\lambda)$, and high correlations (above 0.8) are restricted to the surface 10 m inshore of 125°W (Figures 6b–6d). The vertical extent of high correlations is concordant with the cross-shore thickness of the plume. The dispersion of points for surface (0–5 m) correlations is shown in Figure 7; a more dispersed pattern from the 1:1 line is found inshore of -125°W in two main groups where most data have salinity values over 28.5 (Figures 7c and 7d). These results demonstrate that, in general, the optical characteristics of the offshore CRP are better represented by using several wavelengths from MODIS for accounting the spectral changes of the plume in the cross-shore direction. The effect of a larger smoothing in the MODIS imagery by applying a median filter of 7×7 pixels before the match-ups were extracted

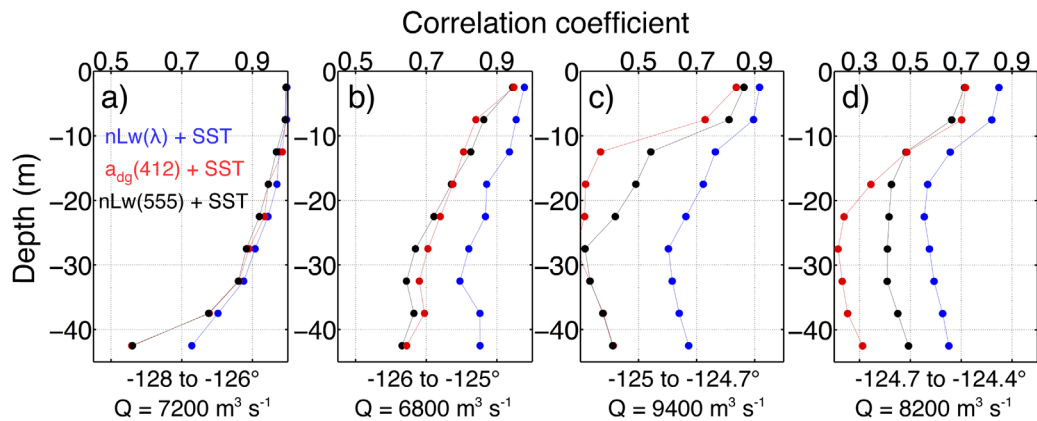


Figure 6. Profiles of correlation coefficients between glider salinity and MODIS-derived salinity estimates off Newport. MODIS-derived salinity has been computed fitting a multivariate regression model of $nLw(\lambda) + SST$, $a_{dg}(412) + SST$, and $nLw(555) + SST$ to glider salinity values at different depths. Results are presented for a particular longitudinal range where surface correlation is maximum: (a) 128°W – 126°W , (b) 126°W – 125°W , (c) 125°W – 124.7°W , and (d) 124.7°W – 124.4°W . The river discharge (Q) value separating two groups of match-up data, for each longitudinal range, is also shown. Thus, each match-up case uses one of two different regression estimates depending on if the river discharge is greater or lower than Q . This grouping by high and low river discharge produced improved correlations.

for the regression analyses reduces the MDS range for a given glider salinity and increases the correlation coefficients, especially inshore than 125°W (Figure 7, bottom).

A reconstruction of MDS was recomputed based on 8 day MODIS composites in order to evaluate major fresh/salty events off Newport during the seven upwelling seasons of study (Figure 8). Even though 8 day composites are not appropriate for resolving rapid plume fluctuations, they represent a short time interval for studying the seasonal-to-interannual variability. Also, 8 day MODIS composites have been shown to be adequate for performing match-ups analyses off central Oregon, with increased data coverage [McKibben et al., 2012]. We used the regression coefficients from the results gathering all data (Table 3) to avoid cross-shore discontinuities in the salinity field from the segments presented in Figures 6 and 7. The MDS algorithm reproduced fairly well the low-salinity events of 2008–2012, and the more salty patterns farther

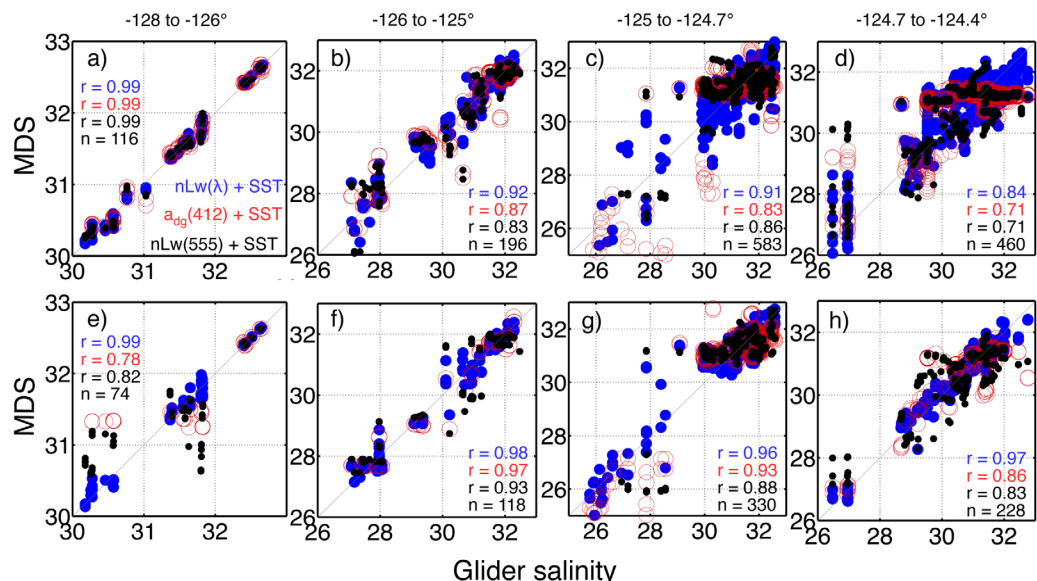


Figure 7. Surface (0–5 m) correlation between glider salinity and MODIS-derived salinity, derived from match-ups after a median filter of (top) 3×3 pixels and (bottom) 7×7 pixels is applied to all MODIS imagery. Longitudinal ranges and river discharge threshold values are the same as in Figure 6, and in the same order from left to right. Note that increased correlation is obtained when using a larger window (7×7 in this case) in the inshore direction. Sharp fronts are consequently smoothed considerably near the coastline which becomes an important limitation for match-ups located around sharp fronts.

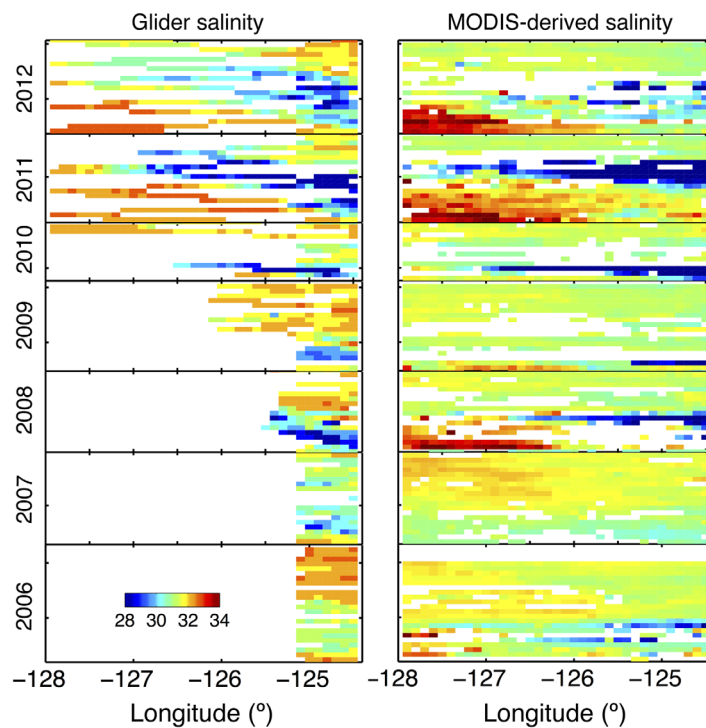


Figure 8. Hovmöller diagrams of (left) average surface (0–5 m) salinity from gliders and (right) MODIS-derived salinity using a multivariate regression analysis (based on $nLw(\lambda) + SST$) with all match-ups. Note that the height of each plot is proportional to the number of days of each upwelling season. Bins of glider salinity and MODIS-derived salinity have been generated averaging all data in 0.1° longitude by 8 days in a cross-shore band of 5 km north and south of NH-line. Thus, gaps in both glider measurements and MODIS composites are considerably reduced.

and Peterson, 2009]. The potential impacts of the plume on the far-field ecosystem, however, are practically unknown. Our glider average profiles suggest that the plume produces a shallower mixed layer, and consequently, chlorophyll concentration exhibits a shallower peak than when there is no plume (Figures 3 and 4). The source of nutrients for this high chlorophyll off Newport is most likely from the upwelling and very reduced from the river flow, considering that; (1) there is elevated mixing in the near-field plume [Nash et al., 2009], (2) most plume nitrate comes from upwelled shelf water [Hickey et al., 2010], and (3) there is no evidence of iron limitation either within or outside the plume [Kudela and Peterson, 2009]. The vertical sections of chlorophyll fluorescence suggest that the inner front of the plume (in conjunction with the upwelling front) plays an important role in promoting the shallow peak of surface chlorophyll over the shelf (Figures 2k and 2l). The fact that the offshore plume is well developed under strong/persistent upwelling conditions does not permit the influence of the plume to be separated from that of upwelling. Maps of Chl a and nFLH confirm the presence of high chlorophyll fluorescence in coastal waters off Oregon during active upwelling with the presence of the offshore plume (Figures 9c and 9d). In contrast, the case without the CRP, after a wind reversal event, shows a more disperse chlorophyll activity with higher values offshore and reduced chlorophyll activity over Heceta Bank (Figures 9g and 9h). Future studies using a biophysical model would better address the role of the plume (e.g., upwelling with CRP versus upwelling without the

offshore in 2011–2012, but these salty offshore regions were clearly overestimated as result of a greater slope in the regression model (Figure 8). The coherent pattern of freshwater in 2008 makes us believe that the high salinity (~ 33 –33.5) farther offshore was a real event not captured by the gliders in 2008 as the gliders did not take measurements that far offshore until 2010.

4. Discussion

4.1. Influence of the Offshore CRP on the Coastal Ecosystem

The influence of the CRP on the coastal margin has been mostly described near the Columbia River mouth [Hickey et al., 2010]. The plume plays a crucial role during periods of delayed upwelling by supplying nutrients, maintaining high rates of primary productivity in new plume waters, and enhancing zooplankton aggregations at the plume fronts [Peterson

Table 3. Regression Coefficients for the Estimation of MDS Off Newport, Central Oregon, From $nLw(\lambda) + SST$ as in Figure 8^a

Q	β_0	$\beta_{(412)}$	$\beta_{(443)}$	$\beta_{(469)}$	$\beta_{(448)}$	$\beta_{(531)}$	$\beta_{(547)}$	$\beta_{(555)}$	$\beta_{(645)}$	$\beta_{(667)}$	$\beta_{(678)}$	β_{SST}
>9400	38.21	4.86	-4.07	-2.70	8.59	-10.19	4.29	-6.33	0.25	8.37	3.30	-0.49
<9400	31.89	1.32	-3.70	3.10	1.61	-10.86	1.54	7.98	-10.55	15.03	-5.28	-0.01

^aNote that the regression model used depends on the river flow (Q ; $m^3 s^{-1}$) for a particular day. This grouping as function of river flow produced the best regression estimates of MDS. The correlation between glider salinity and MDS using these regression coefficients results in $r = 0.78$, $p < 0.05$.

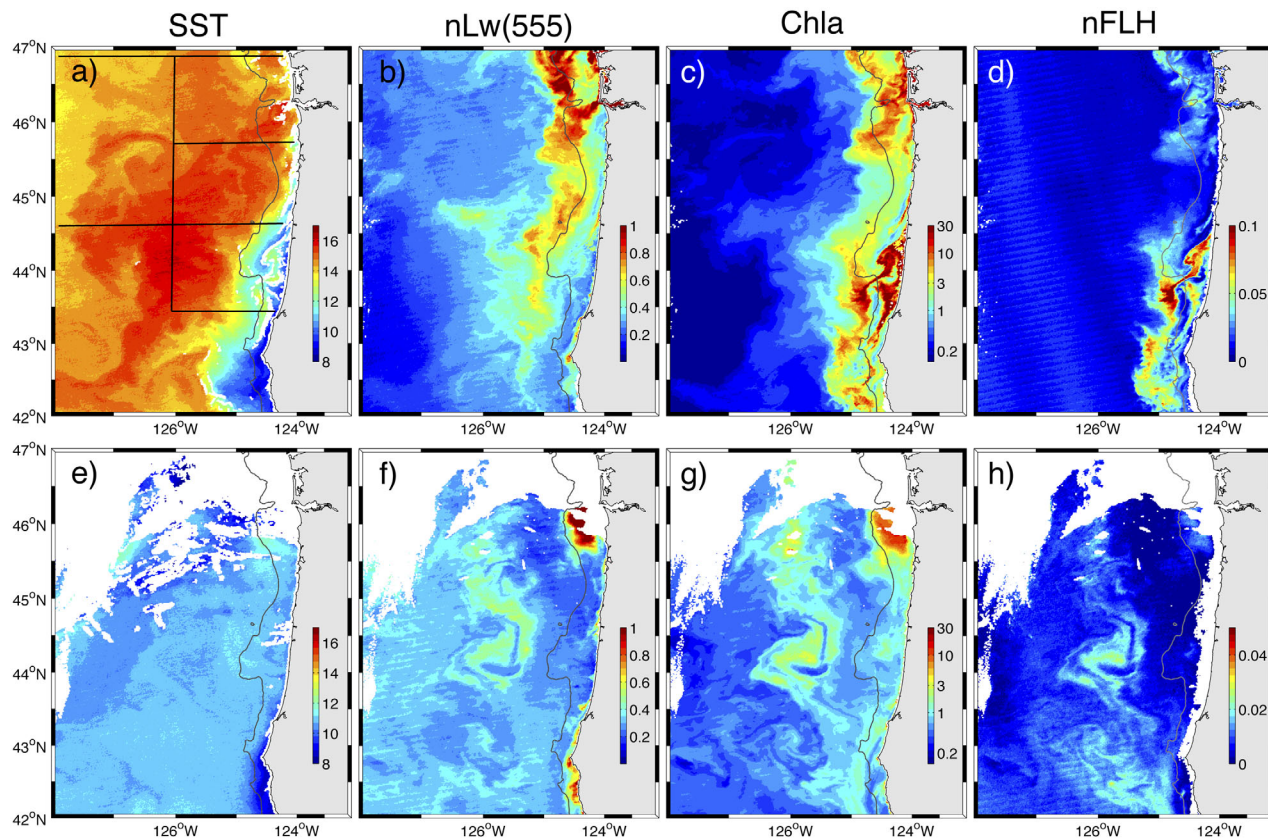


Figure 9. Examples of MODIS composites of (a, e) SST ($^{\circ}\text{C}$), (b, f) $n\text{Lw}(555)$ ($\text{mW cm}^{-2} \mu\text{m}^{-1} \text{sr}^{-1}$), (c, g) Chl *a* (mg m^{-3}), and (d, h) $n\text{FLH}$ ($\text{mW cm}^{-2} \mu\text{m}^{-1} \text{sr}^{-1}$) during a period (top) with and (bottom) without the influence of the offshore CRP off central/southern Oregon. Top (bottom) plots correspond to 6 July 2010 (4 May 2011). Planned glider lines from the Ocean Observatories Initiative (OOI) are shown in black in Figure 9a.

CRP) on the chlorophyll dynamics off Oregon, and the potential role of the plume as a cross-shore barrier during active upwelling (Figure 9d). The CRP has been identified, based on modeling results, as cross-shelf exporter and along-coast barrier for particles transported south from the Washington shelf [Hickey and Banas, 2008; Banas *et al.*, 2009], however, the role of the plume on local production/transport off central/south Oregon has not been tested to date.

4.2. Optical Implications

The change in optical properties off Newport as the CRP is transported southward and offshore [Pak *et al.*, 1970] is evident in the differences in the spectral shape curves between the near-field and offshore plume area (Figures 1c and 5). The differences in $n\text{Lw}(\lambda)$ at the blue bands (400–450 nm) would resemble the decreased influence of CDOM off Newport (less water absorption at these bands) as compared to the near-field area. Lower $n\text{Lw}(\lambda)$ at the green bands suggest that the amount of suspended material is also reduced (Figures 1c and 5). The decreased level of turbidity of the offshore plume, compared to the near-field plume, has implications in the processing procedure of ocean color images. The higher values of $n\text{Lw}(748)$ in the near-field plume (Figure 1c) suggest a considerable influence of high sediment concentrations on the quality of ocean color products—the black pixel assumption does not hold in these cases [Wang and Shi, 2007]. Consequently, studies using ocean color imagery of the near-field plume should use SWIR bands for atmospheric corrections. Also, a new regional algorithm is needed in order to produce accurate satellite Chl *a* retrievals in the presence of the offshore CRP during the productive upwelling season—the offshore CRP shows coherent fields of $n\text{Lw}(555)$ and Chl *a*, which are not supported by the fluorescence distribution (Figures 9b–9d). This is not surprising as default satellite Chl *a* algorithms (e.g., OC3 for MODIS; OC4 for SeaWiFS) do not produce accurate Chl *a* readings in turbid coastal waters with increased CDOM and sediment concentrations [e.g., Dall'Olmo *et al.*, 2005; Gitelson *et al.*, 2007]. Spatial differences in phytoplankton

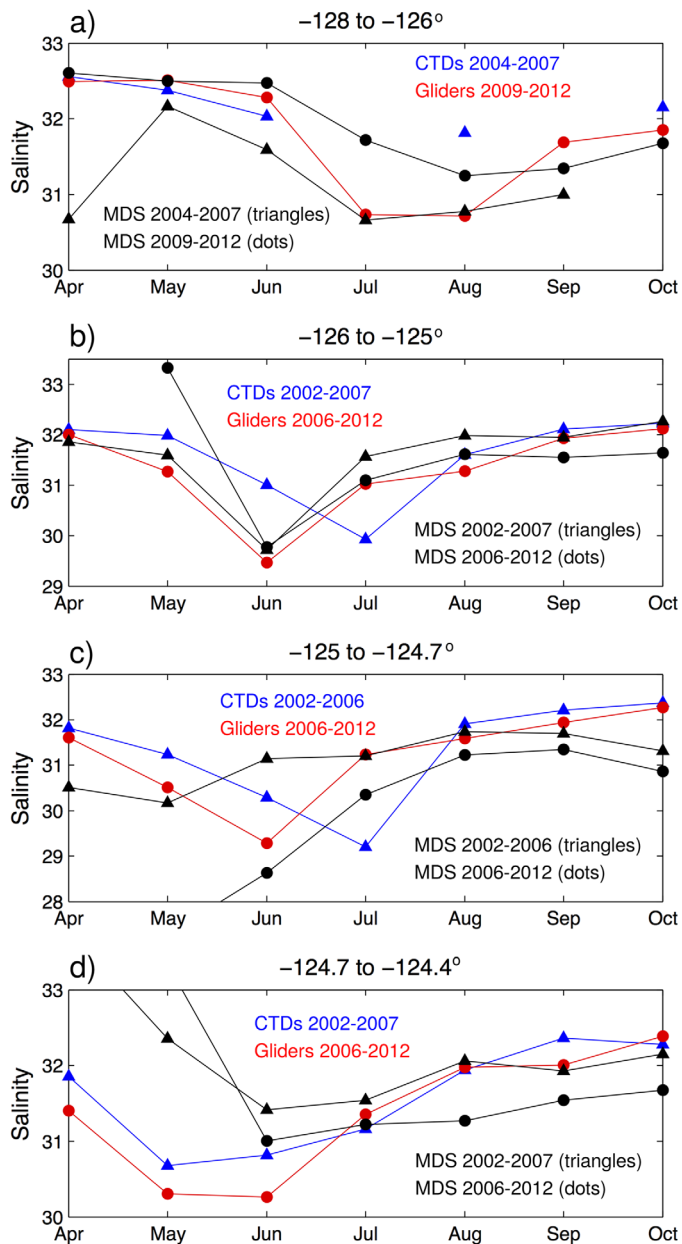


Figure 10. Seasonal cycles (spring-summer) of surface salinity as measured by CTD profiles (2002–2007), glider observations (2006–2012), and MDS algorithms (2002–2007, 2006–2012) off Newport. (a–d) Longitudinal ranges are the same as in Figures 6 and 7.

sion and entrainment into the near-field region can be important during summertime when the river flow is reduced [Spahne *et al.*, 2009]. The use of numerical experiments of river-derived sediment transport [e.g., Rego *et al.*, 2010] would help to address the relative role of particle sinking and turbulent mixing on the cross-shore differential sediment (Figure 1a) and optical signatures (Figure 5) under the influence of the offshore CRP.

Even though the general interannual variability of surface salinity patterns off Newport can be identified through multivariate regression (Figure 8), the low accuracy of particular events (as the end of the upwelling seasons of 2006 and 2008) raises the question if other more sophisticated statistical approaches, such as generalized additive models [e.g., Urquhart *et al.*, 2012] or neural network techniques [e.g., Geiger *et al.*, 2013], would produce better predictions of surface salinity for mapping the offshore CRP. In this regard,

physiology could also, in some extent, account for the spatial differences between Chl *a* and nFLH [e.g., Behrenfeld *et al.*, 2009].

The optical characteristics of the offshore CRP, as seen in the cross-shore direction off Newport (Figures 4 and 5), permit the identification of plume waters from a glider-MODIS analysis. The multichannel approach is an improved option for estimating surface salinity from MODIS, mainly inshore of 125°W where single wavelength products show decreased performance (Figure 6). The lack of high-turbidity signature (e.g., nLw(555)) in the farther offshore region of the plume (128°W–126°W) (Figure 1b), and the need of different regression models to produce improved MDS estimates in the cross-shore direction (Figures 6 and 7), confirm the non-linear spatial variability of optical properties in relation to salinity. This complexity makes it challenging to map the offshore CRP using a single ocean color band as in previous studies [Fiedler and Laurs, 1990; Palacios *et al.*, 2009; Thomas and Weatherbee, 2006]. The cause of the cross-shore differential optical signal (e.g., Figure 5) is more likely the result of a relatively large dispersal of river sediments southward by the upwelling circulation. The CR system allows the finest terrestrial sediments (clay) to be transported far from the river mouth, however, the majority of the sediments from the river is deposited near the river mouth [Wright and Nittrouer, 1995].

Nonetheless, sediment resuspension

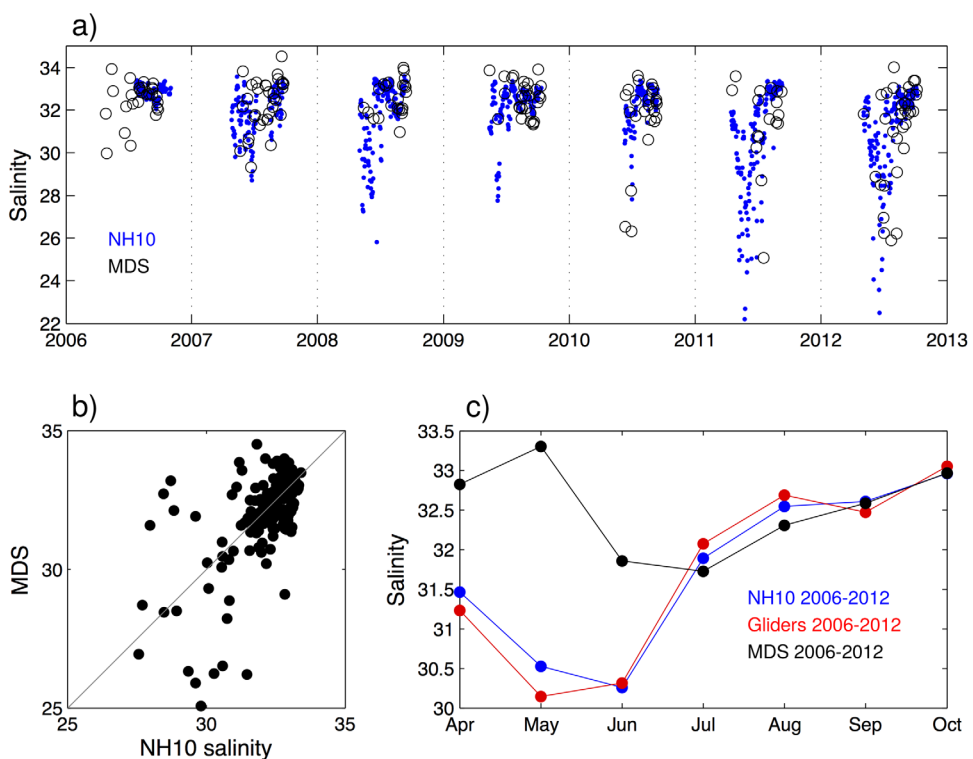


Figure 11. Comparison of surface salinity at/around NH10 mooring; (a) surface salinity from NH10 mooring (blue dots) and MDS (black circles), (b) scatterplot of all coincident surface salinity data between NH10 mooring and MDS, and (c) seasonal cycle of surface salinity from NH10 (blue dots), glider observations (red dots), and MDS algorithm (black dots). MDS algorithm around NH10 mooring is constructed in the same fashion as previous cases; match-up data between MODIS and glider observations are used in a multivariate regression analyses with the best CR flow threshold value separating two groups of data ($Q = 6400 \text{ m}^3 \text{ s}^{-1}$).

surface salinity data from contrasting locations are needed to take into account the whole range of optical variability (from near field to offshore plume) during these events—additional glider data from the Ocean Observatories Initiative (OOI) glider Endurance lines (Figure 9a, black lines) will improve the spatial coverage of our sampling and will help to produce a more robust algorithm for mapping the offshore CRP salinity field. Meanwhile, the interannual evolution (2002 to to-date) of major freshwater events off Newport can be reconstructed by only using 8 day composites of MODIS imagery and the coefficients from Table 3.

4.3. Assessment of MODIS-Derived Salinity Algorithms Off Newport

Additional hydrographic observations from CTD profiles and NH10 mooring are used to evaluate the performance of the MDS algorithms from multivariate regression analyses off Newport (Figures 10 and 11). Following the best regression models from Figure 7 (bottom), the seasonal cycles of surface salinity agreed better during the summer months (July–October) (Figure 10). The drop in surface salinity in July–August is reproduced in the MDS estimates although not quite accurate for the period 2009–2012 (black dots) of glider observations (Figure 10a). The best estimates of MDS, as compared to in situ observations, are presented between the 126°W and 125°W (Figure 10b). In general, surface salinity variability during early spring (April–May) is poorly represented in the MDS estimates inshore than 125°W (Figures 10c and 10d), and consequently, the early arrival of the offshore CRP [e.g., Huyer et al., 2007] would not be quantified/measured properly near the coast by using this MDS algorithm. A longer time series analysis using NH10 salinity data confirms this pattern of erroneous estimates of surface salinity early in the upwelling season (Figure 11c). The larger bias in MDS is evident when waters with low salinity (<31.5) are found over the midshelf (Figures 11a and 11b). A closer look to the dates of match-ups near NH10 reveal that there were no coincident data during April and only a limited number during May and June (two and three match-ups, respectively). Thus, salinity validation is highly constrained by the reduced input from spring data into the regression model, and consequently, not calibrating in a very wide range of salinity and optical variability according to the CRP in springtime.

4.4. Future Studies

Future studies, based on improved maps of MDS for the offshore CRP and glider measurements, would better assist in increasing the understanding of a wide range of plume-related processes. Enhanced along-track satellite salinity data [e.g., *Guerrero et al.*, 2014] and maps of scatterometer wind stress would also provide valuable information of the plume's salinity signature and its variability in relation to wind fields and river flow. Moreover, the warmer signature of the plume (Figure 9a) could have profound implications on air-sea coupling as surface wind stress and curl are strongly modified over sharp SST gradients [*Chelton et al.*, 2004]. On smaller scales, plume fronts are active regions of enhanced vertical mixing dominated by stratified-shear flow instabilities [e.g., *Orton and Jay*, 2005], but in general, small-scale frontal structures and their role on the larger-scale dynamics of river plumes remain poorly understood. Numerical models have not provided sufficient spatial resolution, and observations have been oriented to resolve primarily the vertical flow and salinity structure [*O'Donnell*, 2010].

For the CRP, frontal characteristics have only been described for the near-field region [e.g., *Orton and Jay*, 2005; *Kilcher and Nash*, 2010], by which the structure and dynamics of the offshore plume fronts deserve to be thoroughly investigated. In this aspect, combined MODIS-glider analyses will help to evaluate how the offshore CRP is mixing with ambient waters. Note that not only vertical mixing, but also horizontal mixing could be important—the offshore front of the plume, as seen in visible imagery (Figure 1a), shows salient wave-like features (presumably baroclinic instabilities) which should certainly increase its lateral mixing (Figures 1a and 1b). Furthermore, the plume's inner edge directly interacts with the upwelling front shaping a distinct frontal structure (Figures 2c and 2d). Last, future geostationary ocean color missions focusing on the spectral dynamics of the coastal ocean (i.e., the GEO-CAPE mission) [*Fishman et al.*, 2012] will provide unique opportunities for achieving match-up analyses (*in situ* and satellite) due to the reduced impact of cloud coverage associated with geostationary satellites.

5. Summary

Seven years of concomitant glider and MODIS observations off Newport, central Oregon, provide a large set of optical observations for characterizing the offshore Columbia River plume during the upwelling season. The plume is characterized by high CDOM, backscatter, and chlorophyll fluorescence principally distributed around the base of the plume, which shallows in the inshore direction. MODIS normalized water-leaving radiance spectra of plume water show enhancement at green bands up to ~ 154 km from shore, whereas the farther offshore plume water shows a typical clear open ocean spectral shape. This differential cross-shore distribution of optical properties implies that different multivariate regression models are needed, depending on the offshore position, to estimate surface salinity accurately based on MODIS nLw(λ). The lack of additional glider lines farther north and south of Newport limits our ability for evaluating a single MODIS algorithm to map the full extension of the offshore CRP salinity field. Future data from OOI glider Endurance array and moorings will provide us the necessary input for assessing a MDS algorithm of the offshore CRP off Oregon based on a more sophisticated nonlinear statistical model (e.g., artificial neural network). Future studies may take advantage of this optical characterization for detecting the offshore plume and further investigating its physical structure in relation to dominant forcing mechanisms.

References

- Banas, N., P. MacCready, and B. Hickey (2009), The Columbia River plume as cross-shelf exporter and along-coast barrier, *Cont. Shelf Res.*, 29(1), 292–301.
- Barnes, C. A., A. C. Duxbury, and B. A. Morse (1972), Circulation and selected properties of the Columbia River effluent at sea, in *The Columbia River Estuary and Adjacent Ocean Waters*, edited by A. T. Pruter and D. L. Alverson, pp. 41–80, Univ. of Wash. Press, Seattle.
- Barth, J. A., S. D. Pierce, and T. J. Cowles (2005), Mesoscale structure and its seasonal evolution in the northern California Current System, *Deep Sea Res., Part II*, 52(1), 5–28.
- Behrenfeld, M. J., et al. (2009), Satellite-detected fluorescence reveals global physiology of ocean phytoplankton, *Biogeosciences*, 6, 1–16.
- Blough, N. V., and R. Del Vecchio (2002), Chromophoric DOM in the coastal environment, in *Biogeochemistry of Marine Dissolved Organic Matter*, edited by D. A. Hansell and C. A. Carlson, pp. 509–546, Academic, San Diego, Calif.
- Boss, E., and W. S. Pegau (2001), Relationship of light scattering at an angle in the backward direction to the backscattering coefficient, *Appl. Opt.*, 40, 5503–5507.
- Castelao, R. M., and J. A. Barth (2005), Coastal ocean response to summer upwelling favorable winds in a region of alongshore bottom topography variations off Oregon, *J. Geophys. Res.*, 110, C10S04, doi:10.1029/2004JC002409.
- Cetinić, I., G. Toro-Farmer, M. Ragan, C. Oberg, and B. H. Jones (2009), Calibration procedure for Slocum glider deployed optical instruments, *Opt. Express*, 17, 15,420–15,430.

Acknowledgments

The Ocean Biology Processing Group (Code 614.2) at the GSFC, Greenbelt, MD 20771, makes possible the distribution of MODIS L1 files. Glider data were obtained from the OSU Glider Group data archive (<http://gliders2.coas.oregonstate.edu/gliderweb/>). This research would not have been possible without the continuous hard work of everyone in the OSU Glider Group. The work by Anatoli Erofeev is particularly acknowledged due to his crucial and continuous hard work on glider operations and data processing. The first author (GSS) is supported by a Fulbright and The National Commission for Scientific and Technological Research (CONICYT-Becas Chile) scholarship. J.A.B. and R.K.S. are supported by the U.S. National Science Foundation (NSF) grants OCE-0527168 and OCE-0961999 and National Oceanic and Atmospheric Administration grant NA11NOS0120036. Finally, thanks to the two anonymous reviewers for providing constructive comments that improved this manuscript.

- Chelton, D. B., M. G. Schlax, M. H. Freilich, and R. F. Milliff (2004), Satellite measurements reveal persistent small-scale features in ocean winds, *Science*, 303(5660), 978–983.
- Dall'Olmo, G., A. A. Gitelson, D. C. Rundquist, B. Leavitt, T. Barrow, and J. C. Holz (2005), Assessing the potential of SeaWiFS and MODIS for estimating chlorophyll concentration in turbid productive waters using red and near-infrared bands, *Remote Sens. Environ.*, 96(2), 176–187.
- Del Castillo, C. E., P. G. Coble, J. M. Morell, and J. E. Corredor (1999), Analysis of the optical properties of the Orinoco River plume by absorption and fluorescence spectroscopy, *Mar. Chem.*, 66, 35–51.
- Del Vecchio, R., and A. Subramaniam (2004), Influence of the Amazon River on the surface optical properties of the western tropical North Atlantic Ocean, *J. Geophys. Res.*, 109, C11001, doi:10.1029/2004JC002503.
- Emery, W. J., and R. E. Thomson (2004), *Data Analysis Methods in Physical Oceanography*, 2nd ed., Elsevier, Amsterdam.
- Eriksen, C. C., T. J. Osse, R. D. Light, T. Wen, T. W. Lehman, P. L. Sabin, J. W. Ballard, and A. M. Chiodi (2001), Seaglider: A long-range autonomous underwater vehicle for oceanographic research, *IEEE J. Oceanic Eng.*, 26(4), 424–436.
- Fiedler, P. C., and R. M. Laurs (1990), Variability of the Columbia River plume observed in visible and infrared satellite imagery, *Int. J. Remote Sens.*, 11, 999–1010.
- Fishman, J., et al. (2012), The United States' next generation of atmospheric composition and coastal ecosystem measurements: NASA's Geostationary Coastal and Air Pollution Events (GEO-CAPE) mission, *Bull. Am. Meteorol. Soc.*, 93(10), 1547–1566.
- Franz, B. A., E. J. Kwiatkowska, G. Meister, and C. R. McClain (2007), Utility of MODIS-Terra for ocean color applications, Proc. SPIE 6677, Earth Observing Systems XII, 66770Q, doi:10.1117/12.732082.
- Garau, B., S. Ruiz, W. G. Zhang, A. Pascual, E. Heslop, J. Kerfoot, and J. Tintoré (2011), Thermal lag correction on Slocum CTD glider data, *J. Atmos. Oceanic Technol.*, 28(9), 1065–1071.
- Geiger, E. F., M. D. Grossi, A. C. Trembanis, J. T. Kohut, and Oliver (2013), Satellite-derived coastal ocean and estuarine salinity in the Mid-Atlantic, *Cont. Shelf Res.*, 63, S235–S242.
- Gitelson, A. A., J. F. Schalles, and C. M. Hladik (2007), Remote chlorophyll-a retrieval in turbid, productive estuaries: Chesapeake Bay case study, *Remote Sens. Environ.*, 109(4), 464–472.
- Gordon, H. R. (1997), Atmospheric correction of ocean color imagery in the Earth Observing System era, *J. Geophys. Res.*, 102, 17,081–17,106.
- Guerrero, R. A., A. R. Piola, H. Fenco, R. P. Matano, V. Combes, Y. Chao, C. James, E. D. Palma, M. Saraceno, and P. T. Strub (2014), The salinity signature of the cross-shelf exchanges in the Southwestern Atlantic Ocean: Satellite observations, *J. Geophys. Res. Oceans*, 119, 7794–7810, doi:10.1002/2014JC010113.
- Hickey, B., and N. Banas (2008), Why is the northern end of the California Current System so productive?, *Oceanography*, 21(4), 90–107.
- Hickey, B., S. Geier, N. Kachel, and A. MacFadyen (2005), A bi-directional river plume: The Columbia in summer, *Cont. Shelf Res.*, 25, 1631–1656.
- Hickey, B. M., L. J. Pietrafesa, D. A. Jay, and W. C. Boicourt (1998), The Columbia River plume study: Subtidal variability in the velocity and salinity fields, *J. Geophys. Res.*, 103, 10,339–10,368.
- Hickey, B. M., et al. (2010), River influences on shelf ecosystems: Introduction and synthesis, *J. Geophys. Res.*, 115, C00B17, doi:10.1029/2009JC005452.
- Holte, J., and L. Talley (2009), A new algorithm for finding mixed layer depths with applications to Argo data and Subantarctic Mode Water formation, *J. Atmos. Oceanic Technol.*, 26(9), 1920–1939.
- Huyer, A., P. A. Wheeler, P. T. Strub, R. L. Smith, R. Letelier, and P. M. Kosro (2007), The Newport line off Oregon—Studies in the north east Pacific, *Prog. Oceanogr.*, 75, 126–160.
- Kang, Y., D. Pan, Y. Bai, X. He, X. Chen, C. T. A. Chen, and D. Wang (2013), Areas of the global major river plumes, *Acta Oceanol. Sin.*, 32, 79–88.
- Kilcher, L. F., and J. D. Nash (2010), Structure and dynamics of the Columbia River tidal plume front, *J. Geophys. Res.*, 115, C05S90, doi:10.1029/2009JC006066.
- Kirincich, A. R., J. A. Barth, B. A. Grantham, B. A. Menge, and J. Lubchenco (2005), Wind-driven inner-shelf circulation off central Oregon during summer, *J. Geophys. Res.*, 110, C10S03, doi:10.1029/2004JC002611.
- Klemas, V. (2012), Remote sensing of coastal plumes and ocean fronts: Overview and case study, *J. Coastal Res.*, 28, 1–7.
- Kosro, P. M. (2005), On the spatial structure of coastal circulation off Newport, Oregon, during spring and summer 2001 in a region of varying shelf width, *J. Geophys. Res.*, 110, C10S06, doi:10.1029/2004JC002769.
- Kosro, P. M., W. T. Peterson, B. M. Hickey, R. K. Shearman, and S. D. Pierce (2006), Physical versus biological spring transition: 2005, *Geophys. Res. Lett.*, 33, L22S03, doi:10.1029/2006GL027072.
- Kudela, R. M., and T. D. Peterson (2009), Influence of a buoyant river plume on phytoplankton nutrient dynamics: What controls standing stocks and productivity?, *J. Geophys. Res.*, 114, C00B11, doi:10.1029/2008JC004913.
- Kudela, R. M., et al. (2010), Multiple trophic levels fueled by recirculation in the Columbia River plume, *J. Geophys. Res.*, 37, L18607, doi:10.1029/2010GL044342.
- Large, W. G., and S. Pond (1981), Open ocean momentum flux measurements in moderate to strong winds, *J. Phys. Oceanogr.*, 11, 324–336.
- Litz, M. N., R. L. Emmett, P. J. Bentley, A. M. Claiborne, and C. Barceló (2013), Biotic and abiotic factors influencing forage fish and pelagic nekton community in the Columbia River plume (USA) throughout the upwelling season 1999–2009, *ICES J. Mar. Sci.*, 71(1), 1–4.
- López, R., C. E. Del Castillo, R. L. Miller, J. Salisbury, and D. Wisser (2012), Examining organic carbon transport by the Orinoco River using SeaWiFS imagery, *J. Geophys. Res.*, 117, G03022, doi:10.1029/2012JD001986.
- Marghany, M., and M. Hashim (2011), A numerical method for retrieving sea surface salinity from MODIS satellite data, *Int. J. Phys. Sci.*, 6(13), 3116–3125.
- Maritorena, S., D. A. Siegel, and A. R. Peterson (2002), Optimization of a semi-analytical ocean color model for global-scale applications, *Appl. Opt.*, 41, 2705–2714.
- Mazzini, P. L., J. A. Barth, R. K. Shearman, and A. Erofeev (2014), Buoyancy-driven coastal currents off Oregon during fall and winter, *J. Phys. Oceanogr.*, 44(11), 2854–2876.
- McKibben, S., P. Stratton, D. Foley, T. Peterson, and A. White (2012), Satellite-based detection and monitoring of phytoplankton blooms along the Oregon coast, *J. Geophys. Res.*, 117, C12002, doi:10.1029/2012JC008114.
- Milliman, J. D., and R. H. Meade (1983), World-wide delivery of river sediment to the oceans, *J. Geol.*, 91, 1–21.
- Morel, A. (1974), Optical properties of pure water and pure sea water, in *Optical Aspects of Oceanography*, edited by N. G. Jerlov and E. S. Nielsen, pp. 1–24, Academic, N.Y.
- Morgan, C. A., A. De Robertis, and R. W. Zabel (2005), Columbia River plume fronts. i. Hydrography, zooplankton distribution, and community composition, *Mar. Ecol. Prog. Ser.*, 299, 19–31.

- Nash, J. D., L. F. Kilcher, and J. N. Moum (2009), Structure and composition of a strongly stratified, tidally pulsed river plume, *J. Geophys. Res.*, 114, C00B12, doi:10.1029/2008JC005036.
- O'Donnell, J. (2010), The dynamics of estuary plumes and fronts, in *Contemporary Issues in Estuarine Physics*, edited by A. Valle-Levinson, Cambridge Univ. Press, Cambridge, U. K.
- Orton, P. M., and D. A. Jay (2005), Observations at the tidal plume front of a high-volume river outflow, *Geophys. Res. Lett.*, 32, L11605, doi: 10.1029/2005GL022372.
- Pak, H., G. F. Beardsley, and P. K. Park (1970), The Columbia River as a source of marine light-scattering particles, *J. Geophys. Res.*, 75, 4570–4578.
- Palacios, S. L., T. D. Peterson, and R. M. Kudela (2009), Development of synthetic salinity from remote sensing for the Columbia River plume, *J. Geophys. Res.*, 114, C00B05, doi:10.1029/2008JC004895.
- Palacios, S. L., T. D. Peterson, and R. M. Kudela (2012), Optical characterization of water masses within the Columbia River plume, *J. Geophys. Res.*, 117, C11020, doi:10.1029/2012JC008005.
- Peterson, J. O., and W. T. Peterson (2009), Influence of the Columbia River plume on cross-shelf transport of zooplankton, *J. Geophys. Res.*, 114, C00B10, doi:10.1029/2008JC004965.
- Pierce, S. D., J. A. Barth, R. E. Thomas, and G. W. Fleischer (2006), Anomalous warm July 2005 in the northern California Current: Historical context and the significance of cumulative wind stress, *Geophys. Res. Lett.*, 33, L22S04, doi:10.1029/2006GL027149.
- Qing, S., J. Zhang, T. Cui, and Y. Bao (2013), Retrieval of sea surface salinity with MERIS and MODIS data in the Bohai Sea, *Remote Sens. Environ.*, 136, 117–125.
- Rego, J. L., E. Meselhe, J. Stronach, and E. Habib (2010), Numerical modeling of the Mississippi-Atchafalaya rivers' sediment transport and fate: Considerations for diversion scenarios, *J. Coastal Res.*, 26, 212–229.
- Schofield, O., R. A. Arnone, W. P. Bissett, T. D. Dickey, C. O. Davis, Z. Finkel, M. Oliver, and M. A. Moline (2004), Watercolors in the coastal zone: What can we see?, *Oceanography*, 17, 24–31.
- Schofield, O., J. Kohut, D. Aragon, L. Creed, J. Graver, C. Haldeman, J. Kerfoot, H. Roarty, C. Jones, D. Webb, and S. Glenn (2007), Slocum gliders: Robust and ready, *J. Field Robotics*, 24, 1–14.
- Shi, W., and M. Wang (2009), Satellite observations of flood-driven Mississippi River plume in the spring of 2008, *Geophys. Res. Lett.*, 36, L07607, doi:10.1029/2009GL037210.
- Spahn, E. Y., A. R. Horner-Devine, J. D. Nash, D. A. Jay, and L. Kilcher (2009), Particle resuspension in the Columbia River plume near field, *J. Geophys. Res.*, 114, C00B14, doi:10.1029/2008JC004986.
- Thomas, A. C., and R. A. Weatherbee (2006), Satellite-measured temporal variability of the Columbia River plume, *Remote Sens. Environ.*, 100, 167–178.
- Urquhart, E. A., B. F. Zaitchik, M. J. Hoffman, S. D. Guikema, and E. F. Geiger (2012), Remotely sensed estimates of surface salinity in the Chesapeake Bay: A statistical approach, *Remote Sens. Environ.*, 123, 522–531.
- Wall, C. C., F. E. Muller-Karger, M. A. Roffler, C. Hu, W. Yao, and M. E. Luther (2008), Satellite remote sensing of surface oceanic fronts in coastal waters off west-central Florida, *Remote Sens. Environ.*, 112, 2963–2976.
- Wang, M., and W. Shi (2007), The NIR-SWIR combined atmospheric correction approach for MODIS ocean color data processing, *Opt. Express*, 15, 15,722–15,733.
- Wright, L., and C. Nittrouer (1995), Dispersal of river sediments in coastal seas: Six contrasting cases, *Estuaries*, 18(3), 494–508.